Journal of Alloys and Compounds 854 (2021) 157093

Contents lists available at ScienceDirect

Journal of Alloys and Compounds

journal homepage: http://www.elsevier.com/locate/jalcom

Investigations of the structural, optoelectronic and band alignment properties of Cu_2ZnSnS_4 prepared by hot-injection method towards low-cost photovoltaic applications

Bharat R. Bade [a, b], Sachin R. Rondiya [d, **], Yogesh A. Jadhav [a], Mahesh M. Kamble [c], Sunil V. Barma [a], Sagar B. Jathar [a], Mamta P. Nasane [a], Sandesh R. Jadkar [b], Adinath M. Funde [a, ***], Nelson Y. Dzade [d, *]

[a] School of Energy Studies, Savitribai Phule Pune University, Pune, 411007, India
[b] Department of Physics, Savitribai Phule Pune University, Pune, 411007, India
[c] PDEA'S Anantrao Pawar College, Pirangut, Mulshi, Pune, 412115, India
[d] School of Chemistry, Cardiff University, Main Building, Park Place, Cardiff, CF10 3AT, Wales, United Kingdom

ARTICLE INFO

Article history:
Received 14 June 2020
Received in revised form
1 September 2020
Accepted 6 September 2020
Available online 8 September 2020

Keywords:
Cu_2ZnSnS_4
hot injection method
Cyclic voltammetry
Band alignment
Band offset

ABSTRACT

Cu_2ZnSnS_4 is a promising, versatile and inexpensive quaternary semiconductor with suitable optoelectronic properties for solar energy conversion. In this work, we report the synthesis of CZTS nanocrystals (NCs) using low-cost homemade hot-injection method. Oleylamine was used as both the binder and stabilizer for the CZTS NCs during the growth process. Detailed investigation of the influence of sulphur concentration and reaction temperature on the structural, stoichiometric, morphological, and optoelectronic attributes of CZTS NCs was carried out. The XRD, Raman, and TEM measurements confirm the formation of phase-pure tetragonal kesterite CZTS NCs. The synthesized CZTS NCs exhibit particle sizes in the range of 15–30 nm and display strong optical absorption in the visible region. The nearly optimal chemical composition of the CZTS NCs was confirmed by energy dispersive X-ray spectroscopy. UV–Visible spectroscopy and electrochemical measurements predict the band gap of the CZTS NCs in the range of 1.3–1.6 eV, which is very close to the optimum values for the fabrication of single junction solar cells. The estimated conduction band offset (CBO) and valence band offset (VBO) of the CZTS-3M/CdS heterostructure are predicted as 0.11 and 0.98 eV, respectively, whereas for CZTS-225 °C/CdS heterostructure, CBO and VBO are 0.10 and 1.0 eV, respectively. The small conduction band offset measured at the CZTS/CdS interface are encouraging characteristics for the carrier transport and the deeper understating of band alignment and interface properties provides a hopeful approach for designing higher efficiency and more efficient carrier separation in CZTS solar cells.

1. Introduction

Photovoltaic (PV) technology, which makes use of the super-abundant and freely available Sun's energy to generate electricity, has obvious economic, environmental and societal benefits. However, for PV technology to provide a significant fraction of the world's energy demands, devices must be composed of cheap and readily available materials [1]. In thin film technologies, CIGS, CdTe and thin film silicon solar cells have exhibited 10–25% efficiencies [2–5], but the high cost of solar cell fabrication, particularly that of silicon, and the degradation of the performance over time remain major issues, which prevent their wide-spread deployment into the power grid scale applications [6]. Emerging next generation solar cells based on chalcogenide thin films like CIGS ($CuInGaSe_2$) and CdTe, show terrestrial cell efficiencies of 17.5–21.7% [7,8], but the scarcity, cost and toxicity associated with the In, Ga, and Cd elements present in these cells limit their sustainability in the future. Among the alternative absorber materials to replace CIGS and CdTe, kesterite-copper-zinc-tin chalcogenides Cu_2ZnSnS_4 (CZTS) and $Cu_2ZnSnSe_4$ (CZTSe) have recently emerged as promising

* Corresponding author.
** Corresponding author.
*** Corresponding author.
E-mail addresses: RondiyaS@cardiff.ac.uk (S.R. Rondiya), adinathf@gmail.com (A.M. Funde), DzadeNY@cardiff.ac.uk (N.Y. Dzade).

https://doi.org/10.1016/j.jallcom.2020.157093

candidates to have the capacity to meet or exceed annual world-wide electricity consumption with a significant cost-reduction [9–12]. Kesterite-CZTS compounds are ideally positioned as a next generation PV materials because they combine: (i) near optimum direct bandgaps (1.5 eV for CZTS and 1.13 eV for CZTSSe), (ii) high optical absorption coefficient of ~10^4 cm^{-1} in the visible light region, with predicted theoretical power conversion efficiency (PCE) more than 30% [9,13], and (iii) component elements that are earth-abundant, cheap, and non-toxic. These characteristics make CZTS absorbers promising candidates for scalable production of cost-effective and environment-friendly thin-film photovoltaics [14–16]. In recent years, with increasing research efforts that have focused on improving the stability, interface properties and charge carrier dynamics of CZTS materials, promising power conversion efficiencies exceeding 10% have been achieved [10,11,17].

The development of simple and cost-effective synthesis approaches to fabricate CZTS thin films have also received significant attention. Compared to vacuum based techniques, non-vacuum based chemical techniques for the synthesis of CZTS thin films, are characterized by low-cost and high throughput [18–20]. Yang, C. et al., reported more than 10% efficiency for a CZTS solar cell. With heat treatment, they controlled the charge carrier recombination at the p-n junction and achieved 11% certified efficiency for CZTS solar cell with 730 mV open-circuit voltage [21]. Thin films prepared by solution based non-vacuum methods have demonstrated the highest power conversion efficiency of 12.6% for CZTSe devices [11,22]. The commonly employed physical and chemical techniques used for the synthesis of CZTS material includes RF magnetron sputtering [23], thermal evaporation [24], pulsed laser deposition [25], e-beam evaporation [26], spray pyrolysis [27], sol-gel method [28], electro-deposition [29], etc. Among the above mentioned synthesis techniques, the hot injection method (HIM) has received a great interest for the synthesis of high-quality CZTS nanocrystals. The simplicity, safety, and low-cost associated with the hot injection method makes it suitable for large-scale production of CZTS NCs. Riha et al. reported the synthesis of mono-disperse CZTS NCs using stoichiometric initial precursor concentration at the synthesis temperature of 300 °C by hot injection method [30]. The effect of process temperatures on particle size in the HIM was investigated by Chernomordik et al. [31]. Wang et al. achieve power conversion efficiency of 12.6% for kesterite CZTSSe fabricated using the hydrazine pure-solution approach [11]. The challenges in kesterite photovoltaics has been summarized in recent reports and mentioned very important issues, such as massive deep defects, uncontrolled grain growth, band trailing, unoptimized interfaces, which need to be addressed for better efficiency [32,33]. There are extensive literature reports on the use of CdS as a buffer layer (n-type material) for CZTS solar cell, and all reports provides strong evidence that CdS has all essential properties to form desirable junction with CZTS to achieve efficient carrier transport [34–38]. A deep understating of band alignment and interface properties (band offset) is, however, needed to achieve proper optimization of the CZTS/CdS heterojunction towards improved charge carrier dynamics and device performance. Rondiya et al. reported conduction and valence band offset of 0.10 and 1.21 eV, respectively, from CV measurements and 0.28 and 1.15 eV from the density functional theory calculations [39].

The structural, morphological, and opto-electrical properties of CZTS NCs synthesized by the hot injection method can be controlled by optimizing synthesis parameters such as process temperature, injection temperature, reaction time, precursor concentrations etc. In this communication, we report the successful synthesis of high-quality CZTS NCs in oleylamine (OLA) via the hot injection method. We have primarily focused on optimizing the stoichiometry of the CZTS by varying sulphur concentration during synthesis. Also, the influence of reaction temperature on the structural, morphological, and opto-electrical properties of CZTS NCs was comprehensively investigated and discussed. From our predicted energy band alignment between the CZTS absorber and commonly used CdS buffer material, we provided insights into the transport mechanism of photogenerated charge carriers across the CZTS/CdS interface. The influence of reaction temperature on the crystal structure, which further affects other physicochemical and optoelectronic properties of the CZTS NCs is unraveled. The study provides further understanding of the versatility of CZTS, not just as a traditional absorber layer, but as a charge transport layer.

2. Experimental details

2.1. Chemicals

For the synthesis of the Cu_2ZnSnS_4 (CZTS) NCs, cupric sulphate ($CuSO_4 \cdot 5H_2O$), zinc sulphate ($ZnSO_4 \cdot 7H_2O$), stannous sulphate ($SnSO_4$), sulphur powder, oleylamine (OLA) ($C_{18}H_{37}N$), iso-propyl alcohol $(CH_3)_2CHOH$, toluene ($C_6H_5{-}CH_3$), acetonitrile (ACN), ferrocene, tetra-butyl ammonium per chlorate (TBAP), P_2O_5, were purchased from Sigma-Aldrich and used without any further purification and treatment.

2.2. Synthesis of high-quality CZTS nanocrystals

The colloidal CZTS NCs were synthesized by the hot injection method. Oleylamine solution was used as the solvent, surfactant, and capping ligand. Cupric sulphate ($CuSO_4 \cdot 5H_2O$), zinc sulphate ($ZnSO_4 \cdot 7H_2O$), and stannous sulphate ($SnSO_4$) were used as sources for Cu, Zn, and Sn, respectively. 0.15 M ($CuSo_4.5H_2O$), 0.075 M ($ZnSO_4 \cdot 7H_2O$) 0.075 M ($SnSO_4$), and 10 mL of oleylamine were mixed in a three-neck flask at room temperature. The first neck of flask is connected to vacuum and argon gas via a two-way connector, the second neck was used for injection of elemental sulphur solution and the third neck of flask was used for insertion of a thermocouple to monitor reaction temperature. The resulting solution was heated to 130 °C for 1 h with constant stirring in alternatingly vacuum and argon gas environment, which ensured the complete elimination of air and moisture from the reaction zone. Once the Cu–Zn–Sn-oleylamine complex turned into a light brownish solution, the reaction temperature was raised to 225 °C. Meanwhile, another solution was prepared, for which 1 M sulphur powder was mixed with 5 mL oleylamine in a glass beaker. This sulphur solution was stirred and heated at constant temperature of 80 °C until all the sulphur powder was completely dissolved, and the solution turned to red color. The resulting heated sulphur precursor solution was rapidly injected into the preheated Cu–Zn–Sn-oleylamine complex solution, which immediately change the color from dark brown to black. The schematic of the experimental setup is shown in Scheme 1. The resulting mixture was maintained at the temperature of 225 °C for half an hour, forming a homogeneous black solution. After the reaction was complete, the three-neck flask was taken out from the heating bath and put in a cold-water bath for cooling. The same experiments were repeated in this set for 2, 3, 4 and 5 M sulphur concentrations. To get rid of impurities and unreacted precursors from the CZTS NCs, it was precipitated using 1:8 toluene to propanol mixture. The colloidal CZTS NCs were recovered from the solution by centrifugation at 4000 rpm. The recovered NCs were annealed at 350 °C for 1 h and finally taken for characterization. In an another set of experiments, the reaction temperature was systematically varied from 200 °C to 300 °C, while keeping all other parameters constant as listed in Table 1. The experimental procedure was same for this

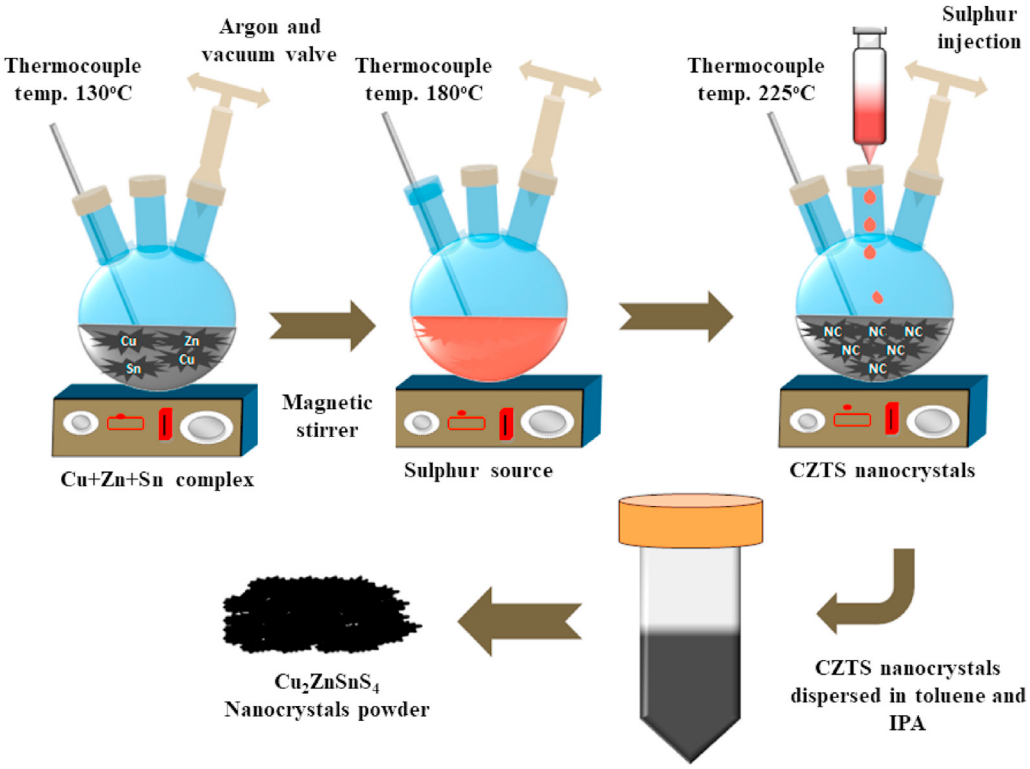

Scheme 1. Schematic of the experimental setup for the synthesis of CZTS NCs using hot injection method.

second set of the experiments in which 4 M sulphur solution were injected into Cu–Zn–Sn-oleylamine complex solution.

2.3. Characterization techniques

The synthesized Cu_2ZnSnS_4 NCs were systematically investigated using different characterization techniques namely, X-ray diffraction (XRD), Raman spectroscopy, UV–Visible spectroscopy, Energy dispersive X-ray spectroscopy (EDS), field emission scanning electron microscopy (FESEM) and scanning electron microscopy (SEM). The average crystallite size, lattice parameter and phase identification of the Cu_2ZnSnS_4 NCs were studied using x-ray diffraction (Bruker D8 Advance, Germany make) with Cu Kα radiation (λ = 1.54 Å). The phase characterization of the as-synthesized samples was obtained by the Raman spectroscopy with "Renishaw Raman Microscope" using argon laser wavelength of 532 nm, in the back-scattering geometry". The optical bandgap of Cu_2ZnSnS_4 NCs were estimated from absorbance spectra measured using a JASCO, V-670 UV–visible spectrophotometer in the range of 200–1400 nm. The Scanning electron microscope (SEM) characterization was performed using the JEOL JSM-6360-LA instrument. The electrochemical measurements for the estimation of band edges and electrochemical band gaps were performed using Metrohm Galvanostat/Potentiostat (Auto lab 100 PGSTAT). The standard 3 electrode system having Au disk, Ag wire, and Pt wire loop as working, reference and counter electrode, respectively. The working electrode is cleaned/polished over the 0.5 μm Al_2O_3 powder and rinsed with copious amount of DI water, followed by potentiodynamically cycling in 0.5 M H_2SO_4, in the potential window (−0.8V–1.5V) to ensure the clean surface of gold. In a typical experiments, the pre-dried 0.341 g of TBAP typically 100 mM in 15 mL pre-dried ACN was transferred to electrochemical cell through silicone septa. The blank cyclic voltammogram were recorded for the reference in TBAP-ACN mixture to ensure there were no peaks corresponding to contamination on the Au electrode. Subsequently the Au electrode was loaded with 100 μL CZTS sample dispersion in ACN (1.0 mg/mL) and vacuum dried. The scan rate was kept constant (100 mV/s) for all measurements. After completion of each set of experiments, the potentials were calibrated using ferrocene as an internal standard with respect to the normal hydrogen electrode (NHE). The band gaps are estimated directly from the cathodic and anodic peak difference. The band edges are extracted from the oxidation and reduction peak potential vs. NHE. These positions are then converted with respect to local vacuum by the standard difference of −4.5 vs NHE [13,40].

Table 1
Deposition parameters employed during reaction.

Synthesis Parameter	SET – I	SET – II
Cupric sulphate	0.15 M	0.15 M
Zinc sulphate	0.075 M	0.075 M
Stannous sulphate	0.075 M	0.075 M
Sulphur powder	**1 M to 5 M**	4 M
Growth Time (min)	120 min	120 min
Reaction Temperature	225 °C	**200 °C – 300 °C**
Annealing Temperature	350 °C	350 °C

3. Results and discussion

3.1. Structural properties

The XRD patterns of the CZTS NCs synthesized at different sulphur concentrations (1–5 M) and reaction temperatures (200 °C–300 °C) respectively, are shown in Fig. 1 (a) and 1 (b). The major diffraction peaks located at 2θ = 28.9°, 33.4°, 47.6°, 56.4°, 69.4°, and 76.7° can be ascribed to the (112), (200), (220), (312), (008) and (332) planes, respectively, of the kesterite phase of CZTS NCs. The positions and intensities of the diffraction peaks are well

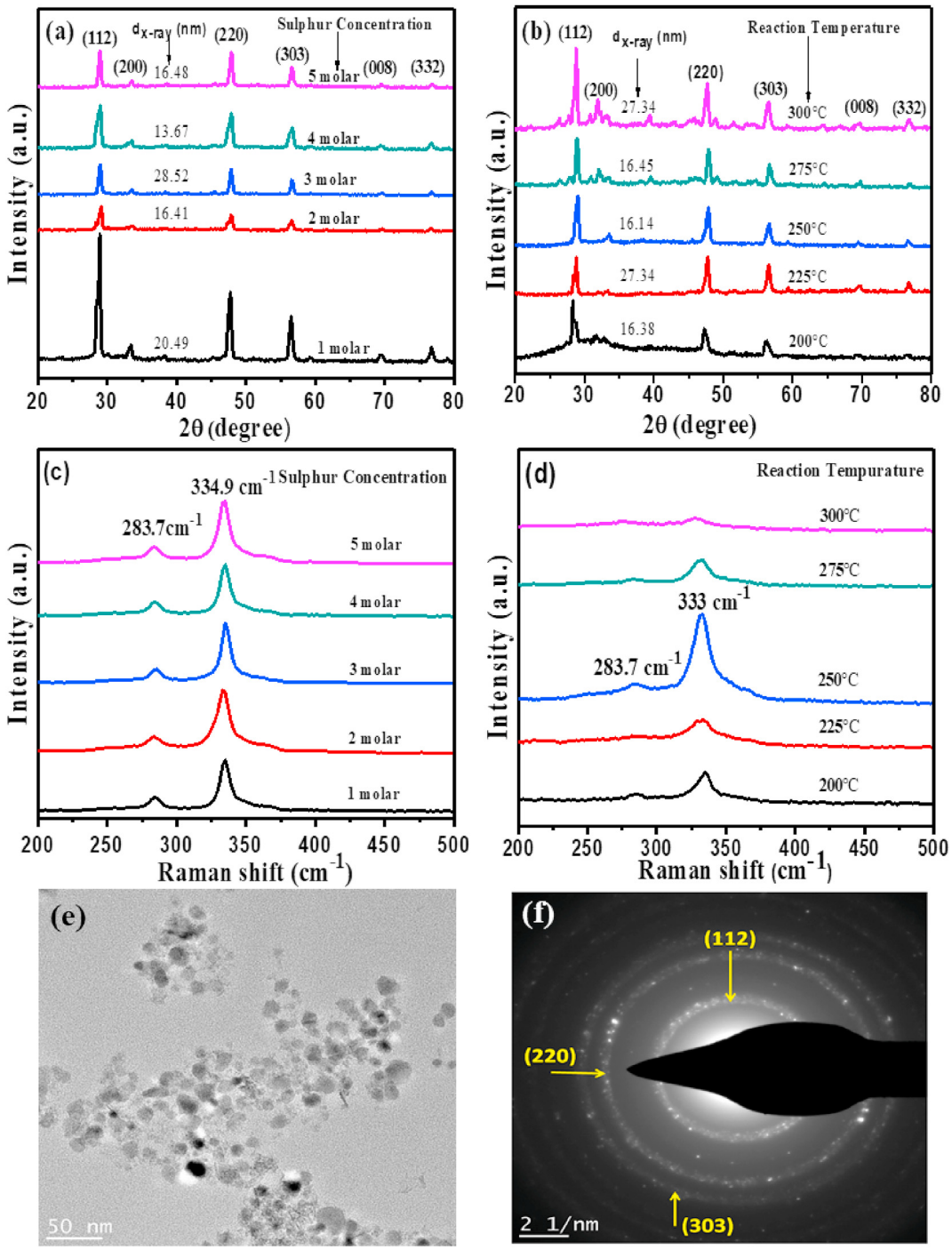

Fig. 1. X-ray diffraction pattern of CZTS powder synthesized at 225 °C (**a)** different sulphur molar concentration (1 M–5 M) (**b)** different reaction temperature (200 °C–300 °C); Raman spectra of CZTS powder synthesized at (c) 225 °C different sulphur molar concentration (1 M–5 M) and (d) different reaction temperature (200 °C–300 °C); (e) TEM image of the 4 M CZTS NCs and (f) SAED pattern of a single CZTS NCs.

matched with the JCPDS card no. #26–0575. No secondary phases like CuS, ZnS, SnS, SnS_2 etc. were detected in all the samples, confirming the formation of high-quality CZTS NCs [41,42]. It is also evident from Fig. 1 (b) that the intensity and sharpness of the (112) plane increases with reaction temperature (up to 250 °C), suggesting that the crystallinity of the CZTS NCs improved gradually with increasing reaction temperature. The observed high intensity and broad shoulder peak located at $2\theta = 28.9°$ in all samples reflects the preferential growth of CZTS along the (112) plane. The variation in crystallite size ($d_{x\text{-}ray}$) of the synthesized CZTS NCs are calculated by measuring the full-width half maxima (FWHM) corresponding to (112) planes using the Debye-Scherrer formula [43]. The calculated crystallite size of the CZTS NCs for set-I and set-II was found to be in the range of 12 nm–28 nm. The maximum crystalline size is observed at 28.5 nm corresponding to the 3 M sulphur concentration in set-1. The observed variations in crystallite size in both sets, can be attributed to the non-uniform lattice strain or different molar concentration of the reaction. Besides, the

nanocrystal size distribution in the hot injection method depends on the process temperature, injection temperature of the sulphur source, reactivity and concentrations of the Cu–Zn–Sn and S precursors, and the type of solvent used [44]. The inter-planar distance of the CZTS NCs for the first-order diffraction is estimated at 3.132 Å, which is very well matched with earlier reported by value of 3.12 Å [45–47]. The lattice constants of CZTS NC for tetragonal structure was calculated using equation (1):

$$1/d^2_{(hkl)} = \left[h^2 + k^2 + l^2\ (a/c)\ 2\right] 1/a^2 \quad (1)$$

where, d is interplanar distance, a and c are a lattice constants and h, k, l are the planes. Shown in Table 2 are the structural parameters of the CZTS NCs prepared with varying sulphur concentration and reaction temperature. The estimated lattice constants for the CZTS kesterite tetragonal structure show good agreement with reported values in the literature [48]. It is clear from the predicted structural parameters coupled with the recorded XRD pattern that all the synthesized CZTS NCs have good crystallinity.

Raman spectroscopy is a unique and powerful characterization technique for the identification secondary phases in a wide range of Raman active materials. Fig. 1 (c) and 1 (d) show the Raman spectra of the CZTS NCs synthesized at different sulphur concentration and reaction temperatures, respectively. CZTS kesterite structures are typically characterized by three main Raman peaks located at 286 cm^{-1}, 336 cm^{-1}, and 371 cm^{-1} [49]. Among these peaks, the strongest peak of CZTS appeared at 336 cm^{-1}, which can be assigned to the A_1 symmetry mode sulphur-metal vibrations in the kesterite lattice [50]. Consistent with previous assignments, we observed two major peaks at 283.7 cm^{-1} and 334.9 cm^{-1} (Fig. 3c) for varying sulphur concentrations, which can be assigned to Raman active mode of the tetragonal kesterite CZTS structure [51]. The high-intensity Raman peak located at 334.9 cm^{-1}, corresponds to the A_1 symmetry mode of a single-phase CZTS NCs [50,52,53]. Similar to the varying sulphur concentrations, the Raman spectra of the CZTS NCs synthesized at varying reaction temperatures (200 °C–300 °C) show Raman peaks at 283.7 cm^{-1} and 333 cm^{-1}. However, the peak intensity decreases and the most intense peak of CZTS NCs shift from 335 cm^{-1} to 332 cm^{-1} with increasing reaction temperature as shown in Fig. 1 (d). The absence of the vibrational modes of cubic ZnS (352 and 275 cm^{-1}) and orthorhombic Cu_3SnS_3 (318 cm^{-1}) confirm the formation of single-phase CZTS by the hot injection method [54,55]. Moreover, energy dispersive X-ray spectroscopy (EDS) composition analysis (Table 3) confirmed that both sets of CZTS NCs have nearly optimal stoichiometric Cu:Zn:Sn:S ratios in all samples. Fig. 1 (e) shows the lower magnification TEM image of the CZTS NCs synthesized with 4 M sulphur concentration, which reveals that the particles are slightly polydispersed. The selected area electron diffraction (SAED) pattern of a CZTS NCs shown in Fig. 1 (f) reveal bright spot patterns that are very well matched to the planes observed from the X-ray diffraction spectra. The average size of the CZTS NCs is found to be 21 nm, also in good agreement with the X-ray diffraction data.

Table 3
Energy dispersive x-ray spectroscopy analysis of CZTS powders synthesized at different sulphur molar concentration (1 M–5 M) and at different reaction temperatures (200 °C–300 °C).

Sample	Cu	Zn	Sn	S
Sulphur molar variation (Set-I)				
CZTS 1 M	23.90	12.35	10.38	53.36
CZTS 2 M	18.76	17.32	10.57	53.34
CZTS 3 M	23.85	14.25	11.11	50.79
CZTS 4 M	25.47	13.59	11.08	49.85
CZTS 5 M	19.38	14.75	11.35	54.52
Temperature variation (Set-II)				
CZTS 200 °C	27.36	17.64	12.5	42.96
CZTS 225 °C	23.19	15.95	11.17	49.70
CZTS 250 °C	24.12	14.92	10.44	50.51
CZTS 275 °C	21.04	11.55	15.49	51.92
CZTS 300 °C	23.91	13.86	11.92	50.32

3.2. Optical properties

The performance of solar cell depends sensitively on the optical properties such as optimum band gap and high absorption coefficient. The optical absorption coefficients of the CZTS NCs were studied in the range of 200–1400 nm. The UV–Visible spectra are recorded on the CZTS NCs dispersed in dimethyl sulfoxide (DMSO). Shown in Figure (2a and 2b) are the absorption spectra of the CZTS NCs synthesized at different sulphur concentration (1 M–5 M) and different reaction temperatures (200 °C–300 °C). All samples show strong absorption in the visible region, indicating that CZTS is a good absorber material in agreement with previous reports [56–58]. The reflectance spectra for the CZTS nanocrystal samples with varying sulphur concentration and reaction temperatures are shown in Fig. 2c and d, respectively. For varying sulphur concentration (Fig. 2c), the lowest reflectance is observed for the samples prepared with 5 M concentration whereas for the temperature variation, the lowest reflectance is observed for 250 °C in the wavelength range of 200–1400 nm. CZTS is a direct band gap material, based on the allowed direct inter band transition. We have estimated the band gap of the synthesized CZTS material using Tauc's relation as reported previously [43] and shown in Fig. 2e and f. The overall band gap for the different sulphur

Table 2
Average grain size (d x-ray), full-width half-maxima (FWHM), inter-planar spacing (d_{hkl}), and lattice strain (ε) for CZTS NCs prepared with varying sulphur concentrations and reaction temperatures.

Sample/Peaks	FWHM (rad)	d (nm)	d_{hkl}	a = b, c (Å)	ε
Sulphur molar variation (Set-I)					
1 M (112)	$6.977*10^{-3}$	20.49	3.132	a = b 5.436, c = 10.550	$1.69*10^{-3}$
2 M (112)	$8.722*10^{-3}$	16.41	3.079	a = b 5.382, c = 10.476	$2.11*10^{-3}$
3 M (112)	$6.977*10^{-3}$	28.52	3.090	a = b 5.382, c = 10.586	$1.68*10^{-3}$
4 M (112)	0.010466	13.67	3.079	a = b 5.382, c = 10.476	$2.53*10^{-3}$
5 M (112)	$8.722*10^{-3}$	16.48	3.090	a = b 5.382, c = 10.586	$2.11*10^{-3}$
Temperature variation (Set-II)					
200° (112)	$8.722*10^{-3}$	16.38	2.850	a = b 5.447 c = 8.476	$2.11*10^{-3}$
225° (112)	$5.233*10^{-3}$	27.34	3.100	a = b 5.393 c = 10.651	$1.26*10^{-3}$
250° (112)	$8.722*10^{-3}$	16.41	3.079	a = b 5.382 c = 10.476	$2.11*10^{-3}$
275° (112)	$8.722*10^{-3}$	16.45	3.090	a = b 5.382, c = 10.586	$2.11*10^{-3}$
300° (112)	$5.233*10^{-3}$	27.34	3.096	a = b 5.404 c = 10.563	$1.26*10^{-3}$

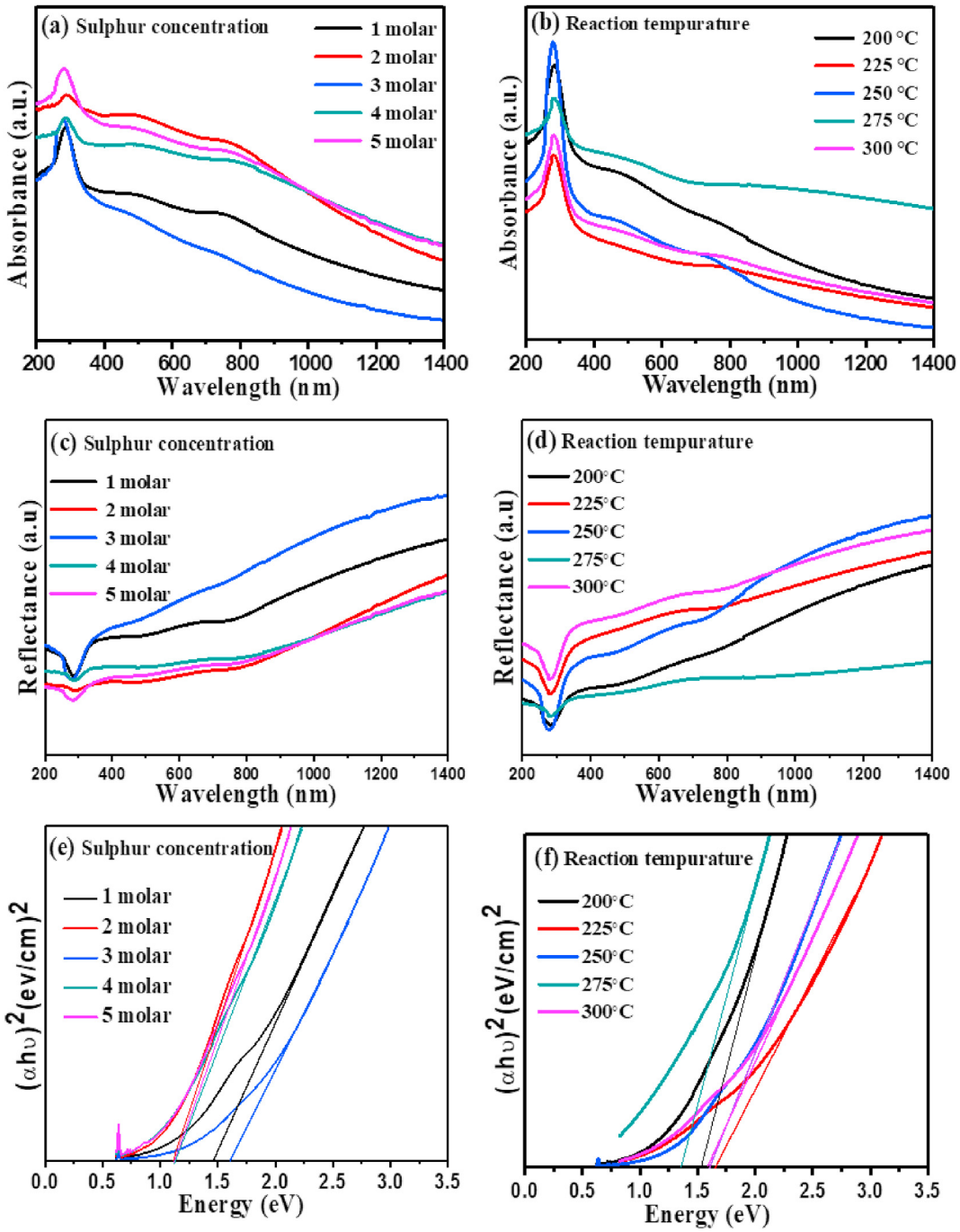

Fig. 2. Absorption spectra of CZTS powder synthesized at (a) different sulphur molar concentration (1 M–5 M) and (b) at different reaction temperature (200 °C–300 °C); Reflection spectra of the CZTS powder synthesized at (c) different sulphur molar concentration (1 M–5 M) and (d) at different reaction temperature (200 °C–300 °C); Tauc Plots of the CZTS powder synthesized at (**e**) different sulphur molar concentration (1 M–5 M) and (**f**) different reaction temperature (200 °C–300 °C).

concentration synthesized CZTS materials was found to be in the range of 1.25–1.55 eV as shown in Table 4. As can be seen from Fig. 2e, slightly higher band gaps are estimated for the 1 M and 3 M concentrations compared to the 2 M, 4 M and 5 M sulphur concentrations. Similarly, the band gap values for the CZTS NCs synthesized by varying reaction temperatures was estimated in the range of 1.45–1.55 eV (Fig. 2f and Table 4), which is well matched with previous experimental reports [57,59–64] and theoretical predictions [65]. The estimated band gaps fall in the optimum band gap range for solar energy conversion in a single-junction device.

The refractive index (n) and extinction coefficient (K_0), which are important properties for optical device and solar cell applications were also determined for the as-synthesized CZTS NCs. *n* is related to the electric polarizability of ions and local field into the material [66,67] whereas the K_0 gives a measures of the fraction of light loss due to scattering and absorption per unit distance in materials [68]. The refractive index (n) of the CZTS NCs was calculated from the reflectance (R) and extinction coefficient (K_0) using equations (2) and (3).

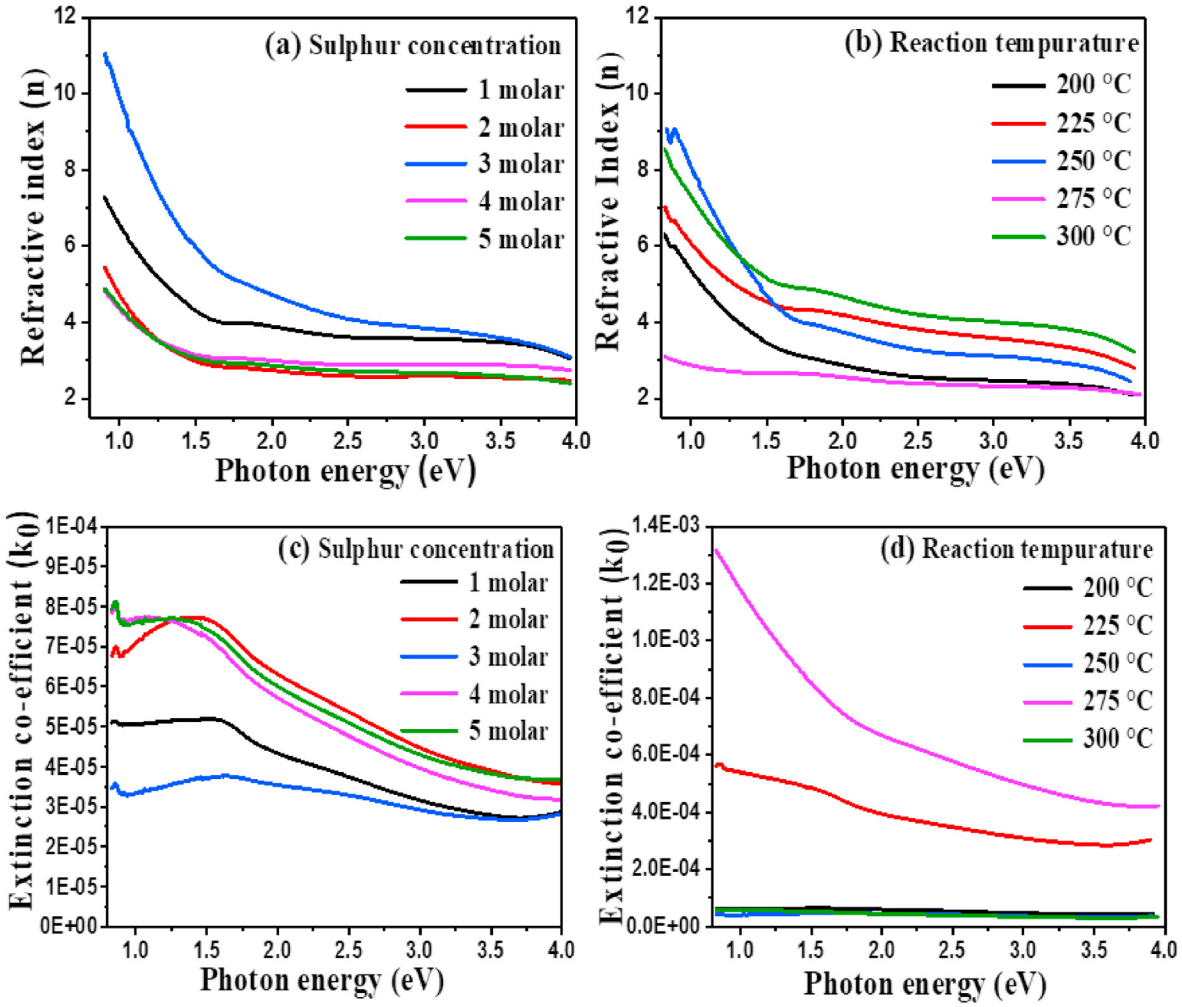

Fig. 3. Refractive index of CZTS powder synthesized at (a) different sulphur molar concentration (1 M–5 M) and (b) at different reaction temperature (200 °C–300 °C); Extinction coefficient of the CZTS powder synthesized at (c) different sulphur molar concentration (1 M–5 M) and (d) at different reaction temperature (200 °C–300 °C).

Table 4
Bandgap (E_g) values of sulphur variation and temperature variation of CZTS NCs.

Molar variation	E_g (eV)	Temperature (°C)	E_g (eV)
CZTS 1 M	1.45	200	1.45
CZTS 2 M	1.24	225	1.52
CZTS 3 M	1.54	250	1.51
CZTS 4 M	1.29	275	1.53
CZTS 5 M	1.26	300	1.54

$$n = \frac{1+R}{1-R} + \sqrt{\frac{4R}{(1-R)^2} - k^2} \quad (2)$$

$$K_0 = \frac{\alpha\lambda}{4\pi} \quad (3)$$

where, R is the reflectance, K_0 is the extinction coefficient, α is the absorption coefficient and λ is the wavelength. The graph of refractive index (n) and photon energy ($\hbar\upsilon$) is shown in Fig. 3 (a) and (b) synthesized CZTS samples with varying sulphur concentration and reaction temperatures, respectively. For sulphur concentration variation (Fig. 3a), the refractive index changed from 10.5 to 3 when the photon energy is varied from 0.6 to 2.5 eV and remains steady for higher photon energies.

In the reaction temperature variation set, the refractive index increases with increasing reaction temperature of CZTS NCs, especially 200 °C, 225 °C, 250 °C and 300 °C. The refractive index varies from 9.0 to 2.5, when photon energy varies from 0.6 to 2.0 eV. The higher refractive index is attributed to the crystallinity in the CZTS NCs, which is evident for the 3 M sulphur concentration in first set and 250 °C reaction temperature in second set. By increasing the sulphur concentration the material becomes denser. So, increasing densification of material causes a decrease in the velocity of the light into the material and leads to increase in the refractive index of the materials [69]. These finding agrees with the X-ray diffraction analysis and further applauded by SEM observation of CZTS NCs. The SEM morphology shows a homogeneous and highly dense surface. Similar observations are also noted in the literature data [70,71]. Fig. 3(c and d) shows the extinction coefficient of CZTS NCs. The extinction coefficient of CZTS NCs increases from 1.0 eV to 2.5 eV photon energy range and decrease in the range of 2.5–4.0 eV photon energy. In the sulphur concentration variation set, the extinction coefficient increases with increasing sulphur concentration, especially 1 M, 2 M, 4 M and 5 M and in the reaction temperature set, the extinction coefficient increases with increasing reaction temperature for 225 °C and 275 °C. The values of K_0 are ranging from 0.0002 to 0.0009. These values of extinction coefficient are low in comparison with reported results, the lower

values are probably due to the weak absorption in the CZTS NCs. The high and low value of the extinction coefficient have direct relation to the absorption of light. The dielectric constant is one of the important intrinsic parameters of the semiconductor to describe the optical behavior of the material for application in solar cell. The dielectric constant has two parts i.e. real part of dielectric constant (ε_r) and imaginary part of the dielectric constant (ε_i). The real part of dielectric constant signifies deceleration of the incident light velocity and imaginary part of dielectric constant signifies interaction of matter from an electric field due to the dipole moment. The real part of dielectric constant (ε_r) and imaginary part of the dielectric constant (ε_i) was calculated by using the values of the refractive index (n) and extinction coefficient (K_0) by using following equations (4) and (5) [72–74]:

$$\varepsilon_r = n^2 - k^2 \tag{4}$$

$$\varepsilon_i = 2nk \tag{5}$$

Fig. 4a–d shows the variation of ε_r and ε_i for the sulphur concentration and process temperature variation as a function of photon energy ($h\upsilon$). The real part dielectric constant increases from 10 to 130 for both sets of samples. It is interesting to note that the values of the real part of dielectric constant are higher than that of

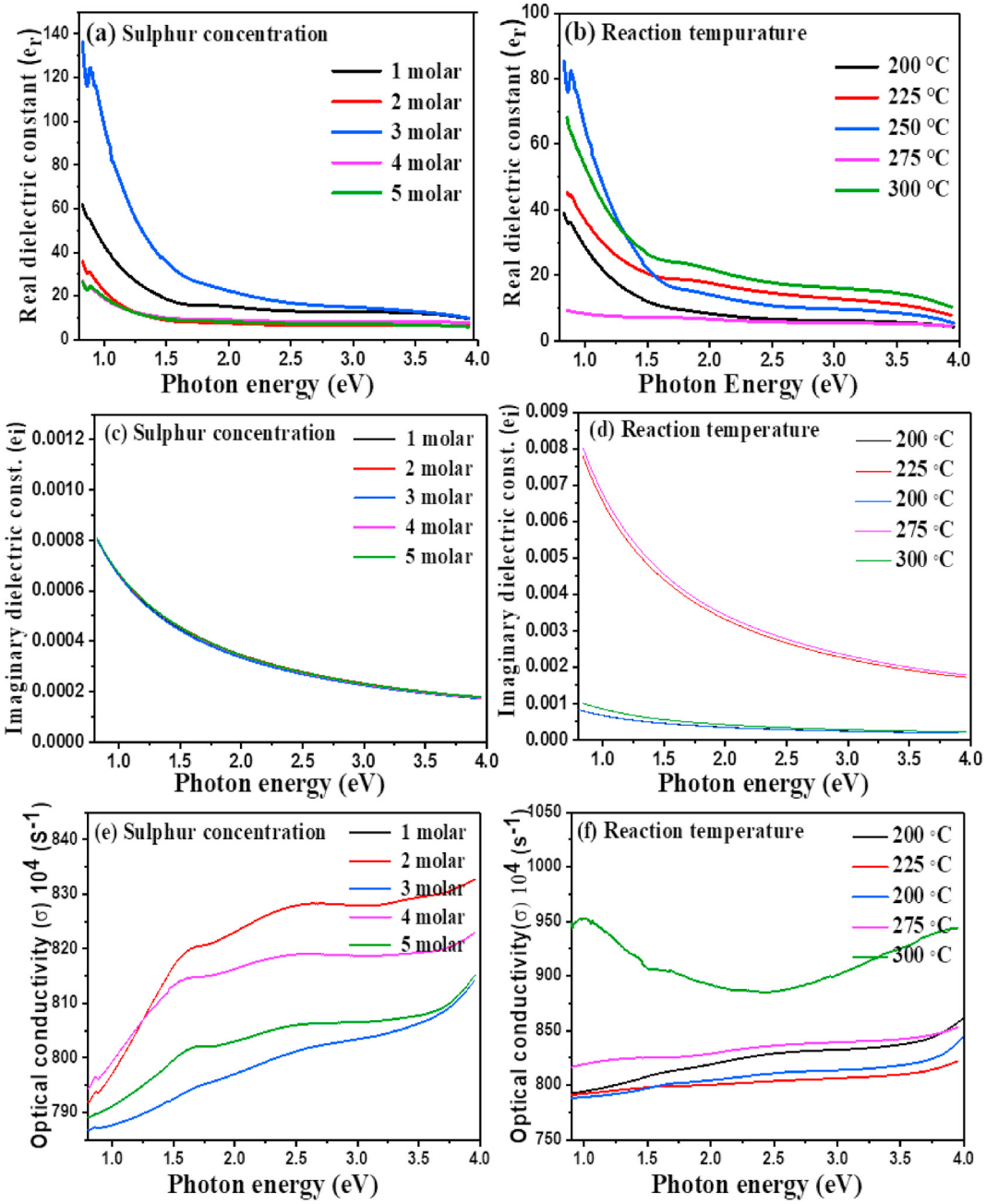

Fig. 4. Real dielectric constant of CZTS powder synthesized at (a) different sulphur molar concentration (1 M–5 M) and (b) at different reaction temperature (200 °C–300 °C); Imaginary dielectric constant of the CZTS powder synthesized at (c) different sulphur molar concentration (1 M–5 M) and (d) at different reaction temperature (200 °C–300 °C); Optical conductivity of the CZTS powder synthesized at (e) different sulphur molar concentration (1 M–5 M) and (f) at different reaction temperature (200 °C–300 °C).

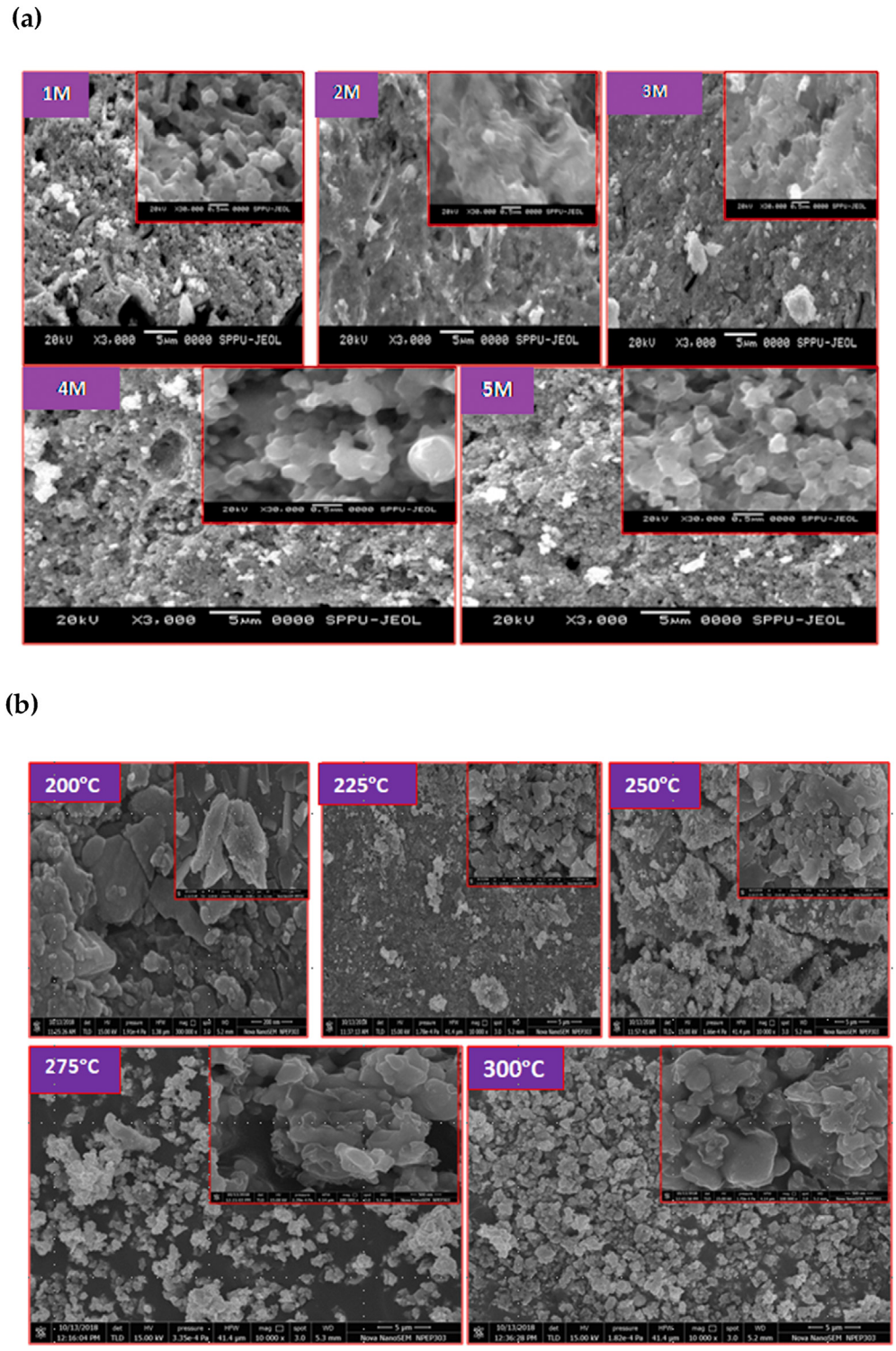

Fig. 5. High resolution magnified FESEM images of CZTS powders synthesized at (a) different sulphur molar concentration (1 M–5 M) and (b) different reaction temperatures (200 °C–300 °C).

imaginary part of dielectric constant and both decreases exponentially with increasing photon energy. The optical response of the material is explicitly studied in term of the optical conductivity. The optical conductivity (σ) of the synthesized CZTS NCs was calculated using the relation: $\sigma = \frac{\alpha nc}{4\pi}$, where, α is absorption coefficient, n is refractive index, and c is speed of light. Fig. 4(e and f) shows the plot of optical conductivity (σ) against photon energy (eV) for the different sulphur concentration and different reaction temperature. It is evident from Fig. 4 (e, f) that the optical conductivity of both sets of samples have very large optical conductivity in the lower wavelength range. These high optical conductivity values can be attributed to the high refractive index and high absorption coefficient of the CZTS NCs. The nature of the plot of "σ_{opt}" is attributed to the photo-excited electrons [75].

3.3. Morphological properties

The low-resolution and high-resolution Field Emission Scanning Electron Microscope (FESEM) images of the CZTS NCs synthesized at varying sulphur concentration (1–5 M) and reaction temperatures (200–300 °C) are presented in Fig. 5a and b, respectively, where we observe significant morphological differences in the CZTS NCs. With increasing sulphur concentration and reaction temperatures, we observed large agglomeration of grains, which has potential implications for photovoltaic application, as larger grains help to reduce recombination rate charge carriers [64,65,76,77]. It is clear from the recorded morphological images of the CZTS powders that the surface morphology is strongly influenced by both the reaction temperature and sulphur molar concentration.

3.4. Cyclic voltammetric measurements

Cyclic voltammetry measurements have been used to estimate the band structure parameters of the prepared CZTS NCs. An argon atmosphere is maintained throughout the electrochemical measurements. In the electrochemical cell, 15 mL of dry acetonitrile (ACN) is used as solvent, 100 mM TBAP as supporting electrolyte and 1 mg/mL solution of CZTS sample in ACN is used to drop-cast on the electrode and used as the working electrode. The blank CV measurement was taken on a bare Au disk electrode and the CV measurement for the CZTS was recorded by drop casting 100 μL CZTS solution on the working electrode, which is dried in vacuum desiccator. Fig. 6 (a) shows the typical CV pattern for the CZTS 225 °C - blue line and CZTS 3 M – red line, drop-casted on the gold electrode. The scan-rate was 100 mV/s. For comparison, the blank

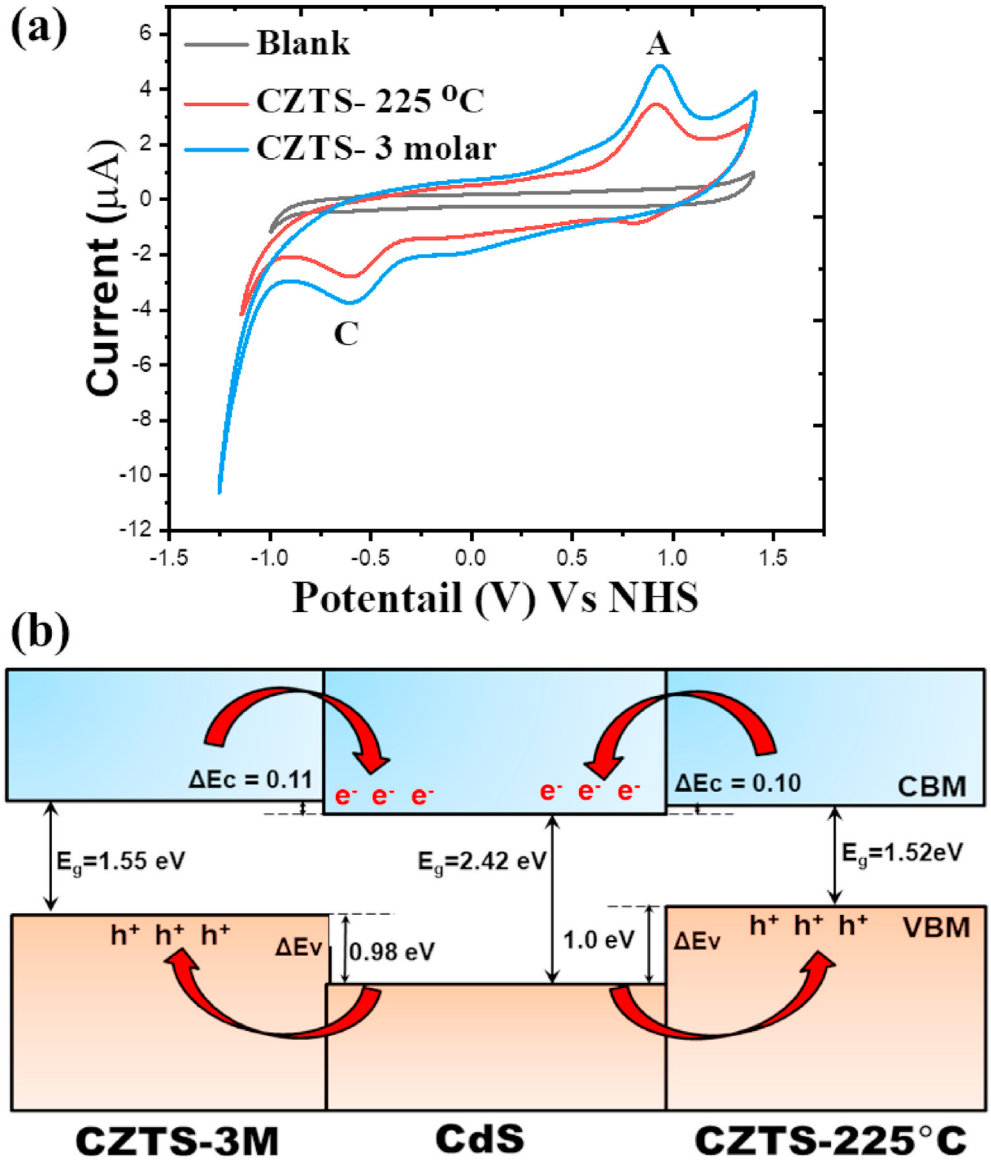

Fig. 6. Cyclic voltammograms for CZTS NCs dispersions, drop-casted on gold electrode for CZTS-225 °C (blue line) and CZTS-3M (red line). The blank run (without CZTS) is shown as a black line. The scan rate was 100 mV/s. Labels A and C indicate prominent anodic and cathodic peaks, observed in the repeated cycles for both the samples. **(b)** Schematic energy band alignment at the CZTS-3M/CdS and CZTS-225 °C/CdS heterojunctions. (For interpretation of the references to color in this figure legend, the reader is referred to the Web version of this article.)

Table 5
Electrochemical band structure parameters from CV measurement on CZTS nanoparticles.

Sample name	Oxidation	Reduction	EC Band gap	Valance Band	Conduction band
CZTS 3 M	0.94	−0.61	1.55 eV	−5.44	−3.89
CZTS 225 °C	0.92	−0.60	1.52 eV	−5.42	−3.90

CV recorded on the bare Au electrode (without CZTS loading) is shown as black line. For the CZTS prepared at 225 °C, a prominent anodic peak at 0.92 V (labelled as A_1) and cathodic peak −0.60 V (labelled as C_1), over and above the background trace is noted in the repeated cycles. Similarly, for the CZTS prepared using the sulphur precursor concentration of 3 M, we have noticed prominent cathodic and anodic peaks at −0.61 V and 0.94 V, respectively. Interestingly, in the 3 M CZTS sample we have observed one additional complementary peak at 0.80 V in the reverse cycle, which corresponds to anodic peak at 0.94 V. The observed complementary peak at 0.80 V in the cyclic voltammogram shows that the CZTS NCs gains electron after oxidation at 0.94 V in the reverse cycle *i.e.*, the CZTS NCs donate electron to the electrode (0.80 V) and get it back in the reverse cycle (0.94 V). These results suggest that the CZTS NCs are more stable in charge transfer condition [78,79]. The oxidation and reduction peaks in the CV are nothing but the electron transfer (donation and acceptance) from valence band and conduction band, which happens because of the applied bias/potential. From the anodic and cathodic peaks, we have deduced the values of valence and conduction band edges (Table 5), which are in very good agreement with previous spectroscopic data [40]. The electrochemical (EC) band gap calculated as the potential difference between the anodic peak A_1 and cathodic peak C_1 is estimated at be 1.55 V for CZTS-225 °C (blue line) and 1.52 V for CZTS-3M (red line). The close agreement between the estimated band gaps obtained from the CV and UV−Visible NIR measurements confirmed the formation of high-quality CZTS NCs by the hot injection method.

3.5. Band alignment investigation at CZTS/CdS interface

Cadmium sulfide (CdS) is a commonly used buffer layer materials for CZTS-based solar devices, hence we have determined the energy band alignment at the CZTS/CdS interface. The magnitude of band offsets controls transport phenomena at the interfaces and characteristics of devices hence the need for their accurate determination. Using the electrochemical band gap and electron affinities for the CZTS (3 M) and CZTS (225 °C) as summarized in Table 5, the band offsets can be estimated. The band gap and electron affinity for the n-type CdS are 2.42 and 4.0 eV, respectively [80]. Shown in Fig. 6 (b) is the schematic energy band alignment at the CZTS-3M/CdS and CZTS-225 °C/CdS interface after heterojunction formation, revealing a type-II band alignment. The conduction band offset (CBO) and valence band offset (VBO) predicted at 0.11 and 0.98 eV, respectively, at the CZTS (3 M)/CdS interface. For the CZTS-225 °C/CdS heterojunction, the CBO and VBO are predicted at 0.10 and 1.0 eV, respectively. The estimated small CBO at the both heterojunctions suggests lesser resistance to electron transport across the CZTS/CdS interface, and hence expected to favor efficient charge carrier separation towards achieving efficient CZTS-based solar devices.

4. Conclusion

Tetragonal kesterite Cu_2ZnSnS_4 (CZTS) NCs were successfully synthesized by the hot injection method. The as-synthesized CZTS NCs were comprehensively characterized using a range of techniques such as XRD, Raman, UV−Vis Spectroscopy, FESEM and EDS all of which confirmed the formation of phase-pure tetragonal kesterite CZTS. The nearly optimal chemical composition of the CZTS NCs was confirmed by our energy dispersive X-ray spectroscopy (EDS) composition analysis. The estimated band gaps from UV−Visible NIR and electrochemical CV measurements are in the range of 1.3−1.6 eV, which is very close to the optimum value for the fabrication of single junction thin film solar cells. Besides, the CZTS samples show strong absorption in the visible region, indicating their suitability as active absorber layer material. We determined a type-II staggered band alignment at the CZTS/CdS heterojunction with smaller conduction band offset (CBO) ~0.1 eV, which is suitable for efficient separation of photo-excited electrons to the CdS and holes to holes to CZTS. We believe that the controlled synthesis parameters for the hot injection method and the generated data presented here will have immediate applications in the synthesis of high-quality CZTS-based materials for device fabrication.

Funding

This research was funded by the UK's Engineering and Physical Sciences Research Council (EPSRC), grant number EP/S001395/1.

CRediT authorship contribution statement

Bharat R. Bade: completed all the samples synthesis, All authors discussed the results, contributed to manuscript write up, and reviewed the manuscript. **Sachin R. Rondiya:** Conceptualization, Writing - original draft, All authors discussed the results, contributed to manuscript write up, and reviewed the manuscript. **Yogesh A. Jadhav:** completed all the samples synthesis, All authors discussed the results, contributed to manuscript write up, and reviewed the manuscript. **Mahesh M. Kamble:** completed all the samples synthesis, All authors discussed the results, contributed to manuscript write up, and reviewed the manuscript. **Sunil V. Barma:** completed all the samples synthesis, All authors discussed the results, contributed to manuscript write up, and reviewed the manuscript. **Sagar B. Jathar:** completed all the samples synthesis, All authors discussed the results, contributed to manuscript write up, and reviewed the manuscript. **Mamta P. Nasane:** completed all the samples synthesis, All authors discussed the results, contributed to manuscript write up, and reviewed the manuscript. **Sandesh R. Jadkar:** Conceptualization, Writing - original draft, All authors discussed the results, contributed to manuscript write up, and reviewed the manuscript. **Adinath M. Funde:** Conceptualization, Writing - original draft, All authors discussed the results, contributed to manuscript write up, and reviewed the manuscript. **Nelson Y. Dzade:** Conceptualization, Writing - original draft, All authors discussed the results, contributed to manuscript write up, and reviewed the manuscript.

Declaration of competing interest

The authors declare that they have no knowm competing financial interests or personal relationships that could have appeared to influence the work reported in this paper.

Acknowledgements

The author BRB and AMF gratefully acknowledge the Ministry of New and Renewable Energy (MNRE), Government of India for fellowship under the National Renewable Energy Fellowship program. SRR and NYD Grant No. EP/S001395/1). AMF acknowledges Exide Industries Limited for the establishment and use of facilities at EXIDE-SPPU Centre of Excellence in Energy Storage at Savitribai Phule Pune University. YAJ thanks SPPU PDF and School of Energy Studies, SPPU for financial support and access to laboratory facilities.

References

[1] C. Wadia, et al., Materials availability expands the opportunity for large-scale photovoltaics deployment, Environ. Sci. Technol. 43 (6) (2009) 2072–2077.
[2] M. Taguchi, et al., 24.7% record efficiency HIT solar cell on thin silicon wafer, IEEE Journal of Photovoltaics 4 (1) (2014) 96–99.
[3] C. Battaglia, et al., High-efficiency crystalline silicon solar cells: status and perspectives, Energy Environ. Sci. 9 (5) (2016) 1552–1576.
[4] L.C. Andreani, et al., Silicon solar cells: toward the efficiency limits, Adv. Phys. X 4 (1) (2019) 1548305.
[5] H.-S. Lee, et al., Enhanced efficiency of crystalline Si solar cells based on kerfless-thin wafers with nanohole arrays, Sci. Rep. 8 (1) (2018) 3504.
[6] N.S. Lewis, et al., Research opportunities to advance solar energy utilization, Science 351 (6271) (2016) aad1920.
[7] M.A. Green, et al., Solar cell efficiency tables (Version 45), Prog. Photovoltaics Res. Appl. 23 (1) (2015) 1–9.
[8] J. Ramanujam, et al., Copper indium gallium selenide based solar cells – a review, Energy Environ. Sci. 10 (6) (2017) 1306–1319.
[9] C. Yan, et al., Cu_2ZnSnS_4 solar cells with over 10% power conversion efficiency enabled by heterojunction heat treatment, Nature Energy 3 (9) (2018) 764–772.
[10] P.D. Antunez, et al., Efficient kesterite solar cells with high open-circuit voltage for applications in powering distributed devices, Nature Energy 2 (11) (2017) 884–890.
[11] W. Wang, et al., Device characteristics of CZTSSe thin-film solar cells with 12.6% efficiency, Advanced Energy Materials 4 (7) (2014) 1301465.
[12] S. Rondiya, et al., CZTS/CdS: interface properties and band alignment study towards photovoltaic applications, J. Mater. Sci. Mater. Electron. 29 (5) (2018) 4201–4210.
[13] S. Rondiya, et al., Structural, electronic, and optical properties of Cu2NiSnS4: a combined experimental and theoretical study toward photovoltaic applications, Chem. Mater. 29 (7) (2017) 3133–3142.
[14] S. Ahmed, et al., A high efficiency electrodeposited Cu_2ZnSnS_4 Solar Cell, Adv. Energy Mater. 2 (2012) 253–259.
[15] P. Dai, et al., Porous copper zinc tin sulfide thin film as photocathode for double junction photoelectrochemical solar cells, Chem. Commun. 48 (2012) 3006–3008.
[16] T. Washio, et al., 6% Efficiency Cu_2ZnSnS_4-based thin film solar cells using oxide precursors by open atmosphere type CVD, J. Mater. Chem. 22 (2012) 4021.
[17] W. Shockley, et al., Detailed balance limit of efficiency of p-n junction solar cells, J. Appl. Phys. 32 (3) (1961) 510–519.
[18] C.J. Hibberd, et al., Non-vacuum methods for formation of Cu(In, Ga)(Se, S)2 thin film photovoltaic absorbers, Prog. Photovoltaics Res. Appl. 18 (6) (2010) 434–452.
[19] S. Pandharkar, et al., Probing the effect of selenium substitution in kesterite-Cu_2ZnSnS_4 nanocrystals prepared by hot injection method, J. Mater. Sci. Mater. Electron. 30 (2019) 14781–14790.
[20] D. Xia, et al., Synthesis and characterization of Cu_2ZnSnS_4 nanocrystals by hot-injection method, J. Mater. Sci. Mater. Electron. 26 (2015) 5426–5432.
[21] C. Yan, et al., Cu_2ZnSnS_4 solar cells with over 10% power conversion efficiency enabled by heterojunction heat treatment, Nat. Energy 3 (2018) 764–772.
[22] G. Brammertz, et al., Characterization of defects in 9.7% efficient Cu2ZnSnSe4-CdS-ZnO solar cells, Appl. Phys. Lett. 103 (16) (2013) 163904.
[23] J.-S. Seol, et al., Electrical and optical properties of Cu2ZnSnS4 thin films prepared by rf magnetron sputtering process, Sol. Energy Mater. Sol. Cell. 75 (1) (2003) 155–162.
[24] H. Katagiri, et al., Development of CZTS-based thin film solar cells, Thin Solid Films 517 (7) (2009) 2455–2460.
[25] K. Moriya, et al., Cu2ZnSnS4Thin films annealed in H2S atmosphere for solar cell absorber prepared by pulsed laser deposition, Jpn. J. Appl. Phys. 47 (1) (2008) 602–604.
[26] H. Katagiri, et al., Preparation and evaluation of Cu2ZnSnS4 thin films by sulfurization of E-B evaporated precursors, Sol. Energy Mater. Sol. Cell. 49 (1) (1997) 407–414.
[27] K. Kumar, et al., Preparation and characterization of spray-deposited Cu2ZnSnS4 thin films, Sol. Energy Mater. Sol. Cell. 93 (8) (2009) 1230–1237.
[28] K. Tanaka, et al., Cu2ZnSnS4 thin film solar cells prepared by non-vacuum processing, Sol. Energy Mater. Sol. Cell. 93 (5) (2009) 583–587.
[29] M. Valdes, et al., Electrodeposited Cu2ZnSnS4 thin films, Electrochim. Acta 128 (2014) 393–399.
[30] S.C. Riha, et al., Solution-based synthesis and characterization of Cu2ZnSnS4 nanocrystals, J. Am. Chem. Soc. 131 (34) (2009) 12054–12055.
[31] B.D. Chernomordik, et al., Rapid facile synthesis of Cu2ZnSnS4 nanocrystals, J. Mater. Chem. 2 (27) (2014) 10389–10395.
[32] F. Liu, et al., Advances in kesterite $Cu_2ZnSn(S, Se)_4$ solar cells, Sci. Bull. 65 (2020) 698.
[33] S. Giraldo, et al., Progress and perspectives of thin film kesterite photovoltaic technology: a critical review, Adv. Mater. 31 (2019) 1806692.
[34] S.R. Rondiya, et al., Effect of bath temperature on optical and morphology properties of CdS thin films grown by chemical bath deposition, Energy Procedia 110 (2017) 202–209.
[35] K. Diwate, et al., Substrate temperature dependent studies on properties of chemical spray pyrolysis deposited CdS thin films for solar cell applications, J. Semiconduct. 8 (2) (2017) 1.
[36] S.R. Rondiya, et al., Synthesis of CdS thin films at room temperature by RF-magnetro sputtering and study of its structural, electrical, optical and morphology properties, Thin Solid Films 631 (2017) 41–49.
[37] A. Kaur, et al., Probing ultrafast charge separation in CZTS/CdS heterojunction through femtosecond transient absorption spectroscopy, J. Phys. Chem. C 124 (36) (2020) 19476–19483.
[38] M.M. Kamble, et al., Optical, structural and morphological study of CdS nanoparticles: role of sulfur source, Nanomater. Energy 9 (1) (2020) 72–81.
[39] S.R. Rondiya, et al., Interface structure and band alignment of CZTS/CdS heterojunction: an experimental and first-principles DFT investigation, Materials 12 (2019) 4040.
[40] Y.A. Jadhav, et al., Voltammetry investigation on copper zinc tin sulphide/selenide (CZTSxSe1-x) alloy nanocrystals: estimation of composition dependent band edge parameters, Sol. Energy Mater. Sol. Cell. 155 (2016) 273–279.
[41] T. Todorov, et al., Cu2ZnSnS4 films deposited by a soft-chemistry method, Thin Solid Films 517 (7) (2009) 2541–2544.
[42] A.V. Moholkar, et al., Studies of compositional dependent CZTS thin film solar cells by pulsed laser deposition technique: an attempt to improve the efficiency, J. Alloys Compd. 544 (2012) 145–151.
[43] B.R. Bade, et al., Investigation of growth mechanism for highly oriented TiO2 nanorods: the role of reaction time and annealing temperature, SN Applied Sciences 1 (9) (2019) 1073.
[44] J. Chang, et al., Colloidal semiconductor nanocrystals: controlled synthesis and surface chemistry in organic media, RSC Adv. 4 (45) (2014) 23505–23527.
[45] V.T. Tiong, et al., Phase-selective hydrothermal synthesis of Cu2ZnSnS4 nanocrystals: the effect of the sulphur precursor, CrystEngComm 16 (20) (2014) 4306–4313.
[46] D. Xia, et al., Characterization of Cu2ZnSnS4 thin films prepared by solution-based deposition techniques, Physics Procedia 48 (2013) 228–234.
[47] S.G. Lee, et al., Structural, morphological, compositional, and optical properties of single step electrodeposited Cu2ZnSnS4 (CZTS) thin films for solar cell application, Curr. Appl. Phys. 14 (3) (2014) 254–258.
[48] N.A. Bakr, et al., Deposition and characterization of Cu2ZnSnS4 thin films for solar cell applications, Int. J. Appl. Eng. Res. 13 (6) (2018) 3379–3388.
[49] S. Levcenko, et al., Free-to-bound recombination in near stoichiometric Cu2ZnSnS4 single crystals, Phys. Rev. B 86 (4) (2012), 045206.
[50] P.A. Fernandes, P.M.P. Salomé, A.F. da Cunha, Study of polycrystalline Cu2ZnSnS4 films by Raman scattering, J. Alloys Compd. 509 (28) (2011) 7600–7606.
[51] K.V. Gurav, et al., Pulsed electrodeposited CZTS thin films: effect of duty cycle, Mater. Lett. 108 (2013) 316–319.
[52] S. Huang, et al., Band positions and photoelectrochemical properties of Cu2ZnSnS4thin films by the ultrasonic spray pyrolysis method, J. Phys. Appl. Phys. 46 (23) (2013) 235108.
[53] M. Huang, et al., Effect of injection rate on the growth of Cu2ZnSnS4 nanoparticles synthesized by hot injection method. IEEE 39th Photovoltaic Specialists Conference, PVSC), 2013.
[54] S.N. Park, et al., Solution-processed Cu2ZnSnS4 absorbers prepared by appropriate inclusion and removal of thiourea for thin film solar cells, RSC Adv. 4 (18) (2014) 9118–9125.
[55] Mokurala, K., et al. Fabrication of Dye Sensitized Solar Cells with Cost-Effective Quaternary Sulfide Counter Electrode. in 2014 IEEE International Conference on Power Electronics, Drives and Energy Systems (PEDES). 2014.
[56] Y. Park, et al., Simultaneous phase and size control in the synthesis of Cu2SnS3 and Cu2ZnSnS4 nanocrystals, CrystEngComm 16 (37) (2014) 8642–8645.
[57] C. Steinhagen, et al., Synthesis of Cu2ZnSnS4 nanocrystals for use in low-cost photovoltaics, J. Am. Chem. Soc. 131 (35) (2009) 12554–12555.
[58] K. Woo, et al., A non-toxic, solution-processed, earth abundant absorbing layer for thin-film solar cells, Energy Environ. Sci. 5 (1) (2012) 5340–5345.
[59] A. Singh, et al., Colloidal synthesis of wurtzite Cu2ZnSnS4 nanorods and their perpendicular assembly, J. Am. Chem. Soc. 134 (6) (2012) 2910–2913.
[60] Q. Guo, et al., Fabrication of 7.2% efficient CZTSSe solar cells using CZTS nanocrystals, J. Am. Chem. Soc. 132 (49) (2010) 17384–17386.
[61] Y. Cao, et al., High-efficiency solution-processed Cu2ZnSn(S,Se)4 thin-film solar cells prepared from binary and ternary nanoparticles, J. Am. Chem. Soc. 134 (38) (2012) 15644–15647.
[62] Q. Guo, et al., Synthesis of Cu2ZnSnS4 nanocrystal ink and its use for solar cells, J. Am. Chem. Soc. 131 (33) (2009) 11672–11673.

[63] C. Persson, Electronic and optical properties of Cu2ZnSnS4 and Cu2ZnSnSe4, J. Appl. Phys. 107 (5) (2010), 053710.
[64] Y. Zhao, et al., Plasmonic Cu2−xS nanocrystals: optical and structural properties of copper-deficient copper(I) sulfides, J. Am. Chem. Soc. 131 (12) (2009) 4253−4261.
[65] G.M. Ford, et al., Earth abundant element Cu2Zn(Sn1−xGex)S4 nanocrystals for tunable band gap solar cells: 6.8% efficient device fabrication, Chem. Mater. 23 (10) (2011) 2626−2629.
[66] R.R. Reddy, et al., Studies on the opto-electronic properties of alkali halides from optical electronegativities, Infrared Phys. 34 (1) (1993) 95−97.
[67] S. Ahmed, et al., Research note: a study of energy gap, refreactive index and electronic polarizability of ternary chalcopyrite semiconductors, Iranian Journal of Physics Research 14 (3) (2014).
[68] K.R. Nemade, et al., Synthesis of MgO nanoparticles by solvent mixed spray pyrolysis technique for optical investigation, Int J Metals (2014), 389416, 4.
[69] K. Sangwal, et al., Relationship between density and refractive index of inorganic solids, J. Phys. Appl. Phys. 20 (4) (1987) 522−525.
[70] N. Bakr, Characterization of a CdZnTe/CdTe heterostructure system prepared by Zn diffusion into a CdTe thin film, J Crystal Growth 235 (2002) 217−223.
[71] R.J. Deokate, et al., Physical and optical properties of sprayed Cu2ZnSnS4 (CZTS) thin film: effect of Cu concentration, J. Mater. Sci. Mater. Electron. 30 (4) (2019) 3530−3538.
[72] K. Punitha, et al., Pulsing frequency induced change in optical constants and dispersion energy parameters of WO3 films grown by pulsed direct current magnetron sputtering, J. Appl. Phys. 115 (11) (2014) 113512.
[73] Kittel, Introduction to Solid State Physics, 7th Ed 2007, p. 688.
[74] Goswami, A., et al., Thin Film Fundamentals 1996: New Age International Pvt. Ltd., New Delhi.
[75] H. Padma Kumar, et al., Optical properties of nanocrystalline HfO2 synthesized by an auto-igniting combustion synthesis, J Asian Ceramic Soc 3 (1) (2015) 64−69.
[76] J.B. Li, et al., Investigating the role of grain boundaries in CZTS and CZTSSe thin film solar cells with scanning probe microscopy, Adv. Mater. 24 (2012) 720−723.
[77] S.N. Park, et al., Nanostructured p-type CZTS thin films prepared by a facile solution process for 3D p−n junction solar cells, Nanoscale 7 (2015) 11182−11189.
[78] S.K. Haram, et al., Quantum confinement in CdTe quantum dots: investigation through cyclic voltammetry supported by density functional theory (DFT), J. Phys. Chem. C 115 (14) (2011) 6243−6249.
[79] Z. Ding, et al., Electrochemistry and electrogenerated chemiluminescence from silicon nanocrystal quantum dots, Science 296 (5571) (2002) 1293−1297.
[80] S.R. Rondiya, et al., Experimental and theoretical study into interface structure and band alignment of the $Cu_2Zn_{1-x}CdxSnS_4$ heterointerface for photovoltaic applications, ACS Appl. Energy Mater. 3 (6) (2020) 5153−5162.